$MoTe_2$: A Type-II Weyl Topological Metal

Zhijun Wang,[1] Dominik Gresch,[2] Alexey A. Soluyanov,[2] Weiwei Xie,[3] S. Kushwaha,[3] Xi Dai,[4] Matthias Troyer,[2] Robert J. Cava,[3] and B. Andrei Bernevig[1]

[1]*Department of Physics, Princeton University, Princeton, New Jersey 08544, USA*
[2]*Theoretical Physics and Station Q Zurich, ETH Zurich, 8093 Zurich, Switzerland*
[3]*Department of Chemistry, Princeton University, Princeton, New Jersey 08540, USA*
[4]*Institute of Physics, Chinese Academy of Sciences, Beijing 100190, China*

(Received 15 December 2015; revised manuscript received 25 February 2016; published 27 July 2016)

Based on the *ab initio* calculations, we show that $MoTe_2$, in its low-temperature orthorhombic structure characterized by an x-ray diffraction study at 100 K, realizes 4 type-II Weyl points between the Nth and $(N+1)$th bands, where N is the total number of valence electrons per unit cell. Other WPs and nodal lines between different other bands also appear close to the Fermi level due to a complex topological band structure. We predict a series of strain-driven topological phase transitions in this compound, opening a wide range of possible experimental realizations of different topological semimetal phases. Crucially, with no strain, the number of observable surface Fermi arcs in this material is 2—the smallest number of arcs consistent with time-reversal symmetry.

DOI: 10.1103/PhysRevLett.117.056805

The ability of gapless band structures to host topological features was first discussed in the context of liquid He [1,2]. It recently became relevant to crystalline materials with the experimental discovery [3,4] of the theoretically predicted [5,6] Weyl semimetals (WSM) in the TaAs family of compounds. In WSMs a topologically protected band crossing of two bands occurs in the close vicinity of the Fermi level forming a gapless node [7–9]. The low-energy Hamiltonian for such semimetals is that of a Weyl fermion [10], which exhibits interesting spectroscopic and transport phenomena such as Fermi arcs [9,11] and the chiral anomaly [7,12–15].

It was recently shown [16] that in materials Weyl fermions come in two flavors: while the type-I Weyl point (WP) (the condensed matter counterpart of the high-energy theory Weyl fermion) is associated with a closed pointlike Fermi surface, its newly proposed type-II cousin [16] appears at the boundary of electron and hole pockets, and has transport properties that are very different from those of the usual, type-I WSM. Another kind of topological metal—a nodal line metal [17–25]—occurs when bands cross along a line in the Brillouin zone (BZ), giving rise to surface states shaped like the surface of a drum [25]. The existence of such a nodal line requires the presence of a symmetry, such as mirror symmetry (or the combination of time reversal and inversion in the absence of spin-orbit coupling (SOC) [26]), in the material.

A WP is associated with a topological charge, since it represents a sink or source of Berry curvature. A nodal line is associated with a Berry phase of π along any mirror-symmetric closed trajectory linking with the line. According to the fermion doubling theorem [27,28] the number of sinks in a crystal has to be equal to the number of sources, meaning that WPs can only appear and annihilate in pairs of opposite topological charge. In nonmagnetic materials the presence of time-reversal symmetry dictates the minimal number of WPs to be four, giving rise to two Fermi arcs on the surface of the material. The WSMs experimentally discovered [3,4,29] and theoretically predicted [5,6,30–32] to date all have more than the minimal number of WPs, as well as a multitude of Fermi arcs, which prevent clean spectroscopy. Of type-I WSMs the TaAs family [5,6] hosts 24 WPs and the recently predicted type-II WSM WTe_2 hosts eight of them between the Nth and $(N+1)$th bands, where N is the total number of valence electrons per unit cell. Below we refer to the bands below band N inclusive as valence, and the ones above as conduction.

In search for other type-II WSMs, it is natural to look at compounds chemically similar to WTe_2. One such compound, $MoTe_2$, in a previously unreported orthorhombic phase was argued to be a strong candidate for another realization of type-II WSM [16,33]. A very recent interesting work [33] reported that orthorhombic $MoTe_2$ also hosts eight type-II WPs in the $k_z = 0$ plane between bands N and $N+1$ (as WTe_2), for the $MoTe_2$ crystal structure measured at 120 K. By further analyzing the $MoTe_2$ structure reported in Ref. [33], we found that in addition there are 16 WPs out of the $k_z = 0$ plane also formed by bands N and $N+1$, located in the immediate vicinity of the Fermi level [34].

In this paper we present the experimental structure of $MoTe_2$ at 100 K and use it to perform first principles and tight-binding calculations of the band structure topology around the Fermi level. Our calculation suggests a different topological physics around the Fermi level than that reported in Ref. [33]: we find only four type-II WPs (which we call W) between bands N and $N+1$ 55 meV above the Fermi level. These WPs give rise to only two clean visible Fermi arcs on the surface of this material.

In this sense $MoTe_2$ represents a "hydrogen atom" of time-reversal invariant WSMs, having the minimal possible number of WPs consistent with time-reversal symmetry. We provide arguments that the difference with the eight WPs in the $k_z = 0$ plane reported in Ref. [33] comes from the high sensitivity of the band structure of $MoTe_2$ to even small changes in lattice parameters—$MoTe_2$ lies on a cusp between a transition from four to eight nodes in between valence and conduction bands in the $k_z = 0$ plane. Indeed, there are small differences in the crystallographic data of Ref. [33] at 120 K and the one reported here at 100 K resulting in the unit cell volume decrease of about 1%, suggesting the possibility of a temperature-driven topological phase transition.

Another recent work [35] predicts the existence of WPs in Mo doped WTe_2. That prediction is obtained by interpolating between the tight-binding models of WTe_2 and a theoretically relaxed orthorhombic $MoTe_2$. Such interpolation represents a very strong approximation for the band structure of a doped compound, which, together with the above discussed sensitivity of the WPs to even small differences in the experimental crystal structure, makes the predictions of the work [35] unreliable. More valuable discussions about strain-driven topological phase transition are presented in the Supplemental Material [36].

Moreover, in metals it is important to look at other topological features near the Fermi level, not only those formed between valence and conduction bands, since the occupation becomes a function of crystal momentum k in this case [61], and we find many such additional features in $MoTe_2$. Inspection of crossings between bands other than N and $N+1$, occurring close to the Fermi level, reveals many additional topologically protected crossings formed by the conduction bands $N+1$ and $N+2$, including line nodes and WPs, some of which (20 in total) are close in energy to the W points (see details in Supplemental Material [36]). We find also two nodal lines close to the Fermi level, formed by the valence bands $N-1$ and N, protected by mirror symmetry. Unlike W points that are formed at the boundary of electron and hole pockets, the additional topological features arise at the touching points of two pockets of the same carriers. Thus, despite a complex topological band structure, the surface Fermi arcs arising due to the four type-II W points are rather clean and should be easy to see in spectroscopic experiments, while the surface states associated with the additional topological crossings overlap with surface projections of the bulk states.

We grew samples by slow cooling and performed diffraction measurements at 100 K. Our results establish that $MoTe_2$ has a new low temperature orthorhombic $1T'$ phase (as was previously reported in [33]), which we designate as the γ phase (more details can be found in the Supplemental Material [36] for the full structure characterization). Using this crystallographic data, we perform *ab initio* calculations based on the density functional theory (DFT) [62,63] and the generalized gradient approximation (GGA) for the exchange-correlation potential [64]. We first compute the band structure of $MoTe_2$ without spin-orbit coupling, as illustrated in Fig. 1(b). We find two mirror-protected nodal lines in the $k_y = 0$ plane (more details in the Supplemental Material [36]) and 12 WPs formed by valence and conduction bands, 4 of which are located in the $k_z = 0$ plane (W1 points) and 8 are out of that plane (W2 points), as shown in Table I.

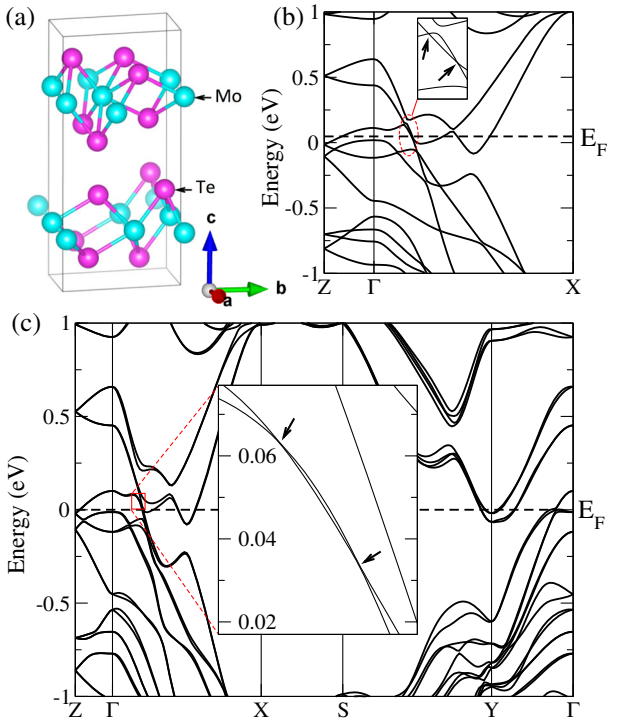

FIG. 1. Atomic and electronic structure of $MoTe_2$. (a) The orthorhombic crystal structure of Td-$MoTe_2$ with Te atoms forming a distorted octahedron around Mo atoms. (b) The band structure of $MoTe_2$ in the absence of spin-orbit coupling. The arrows indicate two crossing points as part of the nodal line. (c) The band structure of $MoTe_2$ with spin-orbit coupling. The inset shows crossings between the $(N-1)$th and Nth bands which are part of a nodal line.

The strong SOC of Mo $4d$ and Te $5p$ states which dominate the physics around E_F significantly changes the band structure as shown in Fig. 1(c). We first elucidate the

TABLE I. WPs of $MoTe_2$. The positions (in reduced coordinates k_x, k_y, k_z), Chern numbers, and the energy relative to the E_F are given. W1 and W2 are the WPs formed by bands $N/2$ and $N/2+1$ in the absence of SOC, while W are the WPs formed by bands N and $N+1$ with full SOC. The coordinates of the other points are related to the ones listed by the reflections $M_{x,y}$.

Weyl points	Coordinates $(k_x(2\pi/a), k_y(2\pi/b)k_z(2\pi/c))$	Chern number	$E-E_F$ (meV)
W1	(0.1819, 0.1721, 0)	+1	−38
W2	(0.1300, 0.0793, ±0.298)	−1	−18
W	(0.1011, 0.0503, 0)	+1	+55

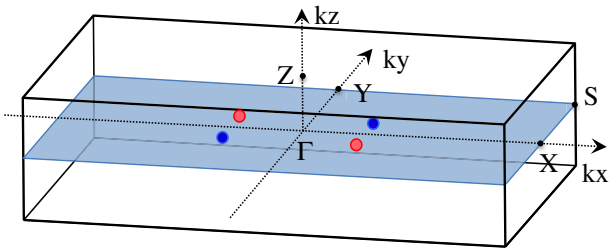

FIG. 2. Weyl points in the Brillouin zone of $MoTe_2$. Four Weyl points formed by bands N and $N+1$ in the Brillouin zone are shown. The blue and red colors indicate Chern numbers $+1$ and -1 respectively.

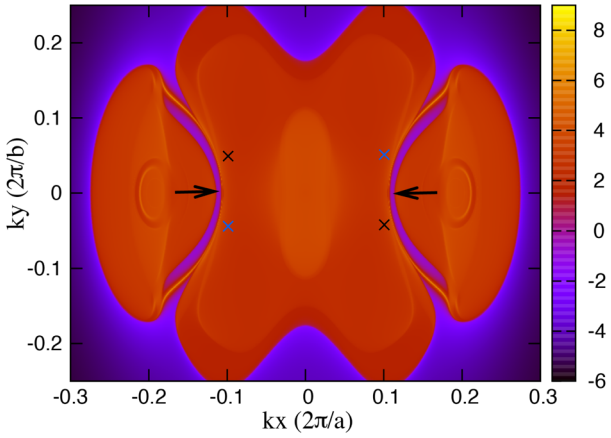

FIG. 3. Spectral function of the (001) surface of the orthorhombic $MoTe_2$ at 20 meV below the Fermi level. A projection of a big holelike pocket is in the center, with the projections of the electron pockets to the left and to the right from it. In the gap of these two kinds of pockets, topological Fermi arcs are marked with arrows. The WPs' projections are denoted by x, with blue and black colors indicating Chern numbers $+1$ and -1, respectively.

topological crossings between valence and conduction bands. The two nodal loops present without SOC become fully gapped. The structure of WPs also changes significantly: the WPs at $k_z \neq 0$ disappear, while only four WPs are found in the $k_z = 0$ plane, still allowed by the C_{2T} symmetry [16,26] (see symmetries in the Supplemental Material [36]). The coordinates of these points (W) are given in Table I. Their location and Chern numbers (see Supplemental Material [36] for the details of Chern number calculation) are illustrated in Fig. 2. The separation between the nearest points with opposite Chern numbers in the unstrained $MoTe_2$ is $\approx 10\%$ of the reciprocal lattice constants $|G_y|$ meaning that the topological Fermi arcs should be easily observable in this material. While, as shown below, other topological gapless features show up very close to the E_F in between bands other than N and $N+1$, it is the W WPs that are most important as they give rise to the only Fermi arcs not superimposed on bulk states upon surface projection.

We computed topological invariants to establish the existence of the WPs, and to prove that no additional WPs are present in between the valence and conduction bands. The first invariant is the Chern number, associated with each of the WPs, which was computed both from the Wannier-based tight-binding model [65,66], and directly from first-principles calculations [67] (see Supplemental Material [36]). The result of this calculation is illustrated in Table I and Fig. 2, where the WPs and their Chern numbers are shown in the BZ.

Further insight into the topology of the Bloch bands of $MoTe_2$ is obtained by computing the $\mathbb{Z}_2$ invariant of the lowest N bands on the time-reversal symmetric planes $k_i = 0,\ \pi$. The $k_z = 0$ plane contains the WPs and is gapless; hence no such invariant can be defined on this plane. The other five planes, however, are gapped between bands N and $N+1$. Of these planes only the $k_y = 0$ one has a nontrivial $\mathbb{Z}_2$ invariant. This means that the $k_y = 0$ cut of the BZ is analogous to the 2D BZ of a quantum spin Hall insulator that carries an odd number of Kramers pairs of edge states. The lack of a nontrivial $\mathbb{Z}_2$ invariant on all the other planes implies the existence of disconnected Fermi surfaces. Notice that a connected Fermi sea of the surface states, be it strong or weak topological or trivial insulator, does not lead to only one nontrivial $\mathbb{Z}_2$ index on a high symmetry plane. Figure 3 shows the surface spectral function for the (001) surface of $MoTe_2$, and topological Fermi arcs crossing the $k_y = 0$ plane are clearly visible.

In type-I WSMs tuning the Fermi level to the energy of the WP results in the surface Fermi arcs connecting projections of the WPs on the particular surface. Type-II WPs appear at the boundary between the pockets, when E_F is tuned to the WP energy; hence projections of bulk carrier pockets necessarily appear in the surface electronic density of states irrespective of the Fermi energy in relation to the WP. The Fermi arcs can in this case be hidden within the projection of the bulk pockets on the surface, but they can still be revealed by tuning the chemical potential (see Supplemental Material [36]). This is illustrated for $MoTe_2$ in Fig. 3, where we chose a spectroscopically reachable value for the chemical potential of -20 meV below E_F. The clean Fermi arcs have been revealed in the angle-resolved photoemission spectroscopy measurement [68]. A projection of a big holelike bulk pocket is seen in the center of the surface BZ, with the projections of the electron pockets to the left and to the right from it. Unlike the case of type-I WSMs, where a Fermi arc connects surface projections of WPs of opposite chirality, the Fermi arcs illustrated in Fig. 3 are of a different nature.

The projections of the W WPs are within the projected hole pocket, and all the Fermi pockets have zero Chern numbers, so that in general no Fermi arcs connecting different pockets should appear. However, any (k_x, k_z) cut of the BZ in between two adjacent W points ($|k_y| < 0.0503$) has to exhibit the quantum spin Hall effect, meaning that a Kramers pair of surface states connecting valence and conduction states has to appear in the gap between them, resulting in topological Fermi arcs. Since the arc cannot appear without being connected to projections of WPs or carrier pockets, for $|k_y| > 0.0503$ it is the

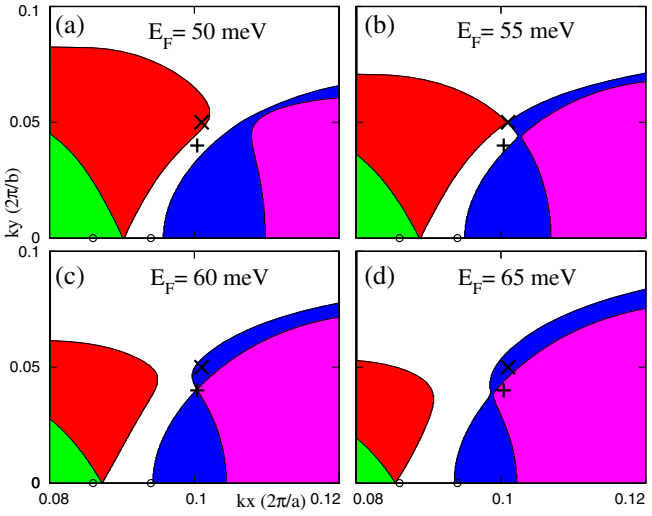

FIG. 4. Contour plot of the bulk Fermi surface at $k_z = 0$ for different values of E_F. The Weyl point W between bands N and $N+1$ is designated with a $\times$ sign, while the Weyl point between bands $N+1$ and $N+2$ is shown as a $+$ sign. The circles mark the crossings of the plane with a nodal line formed by bands $N-1$ and N. Pockets formed by bands $N-1$, N, $N+1$ and $N+2$ are shown in green, red, blue, and cyan correspondingly.

topologically trivial state that continues the arc to merge it into the electron pocket (see Supplemental Material [36] for illustrations). The resultant two Fermi arcs represents the cleanest observable consequence of the type-II WPs.

A cross section of the bulk Fermi surface in the $k_z = 0$ plane around the W points is illustrated in Fig. 4. The Fermi surface consists of two hole (p) and four electron (n) pockets. The latter form two pairs located to the left (not shown) and to the right (shown) of the p pockets. When E_F is below the position of the W [panel (a)] p and n pockets come in pairs of interpenetrating sheets. All the W WPs are inside the p pocket. Upon increasing E_F the p and n pockets approach each other and eventually touch at W [panel (b)]. Further increase of E_F splits the pockets again, but now W is inside the n pockets [panels (c) and (d)]. At all times all the pockets have zero Chern number, enclosing an equal number of WPs with opposite chiralities.

While this concludes the analysis of the WPs between the bands N and $N+1$, $MoTe_2$ exhibits several other topologically protected crossings close to the Fermi level. Even though none of these topological features impact the surface states spectroscopy shown in Fig. 3, as they project inside bulk bands on the surface, we analyze them here for completeness. At only 2 and 5 meV above W, two new quartets of WPs exists between the bands $N+1$ and $N+2$ in the $k_z = 0$ plane. One of these points is clearly seen in Fig. 4(c) occurring at the touching points of the two n pockets. Calculation of additional topological invariants further confirmed the existence of these WPs.

Furthermore, the inset of Fig. 1(c) shows crossings between bands N and $N-1$ occurring on the high symmetry line ΓX. Symmetry considerations [26] indicate that such crossings on a high-symmetry plane can only occur if a line node is present in the mirror plane $k_y = 0$ of the BZ. Indeed, we find that these bands have different glide plane M_y eigenvalues and two line nodes exist in the $k_y = 0$ plane related by mirror M_x. A further check of the topological nature of this ring is obtained by computing the Berry phase of a loop trajectory that links with the nodal line. We find this to be equal to π, as expected for a nodal line.

In conclusion, based on the DFT calculations, we have studied in detail the topological properties of a new orthorhombic γ phase of $MoTe_2$, which has been experimentally characterized. The *ab initio* calculations suggest that unlike the α and β phases, the γ phase hosts a multitude of topological features around the Fermi level including type-II WPs and nodal lines. We found that the WPs between the Nth and $(N+1)$th bands come in a single quadruplet, the smallest number allowed by time-reversal symmetry. This allows for a particularly clean Fermi arc structure on the surface of $MoTe_2$, which should be readily observable in spectroscopic measurements [68]. Other WPs and nodal lines between different other bands also appear in $MoTe_2$, but their spectroscopic signatures on the surface overlap with those of the projected bulk Fermi surfaces.

We thank Binghai Yan for helpful discussions. This work was supported by NSF CAREER DMR-095242, ONR-N00014-14-1-0330, ARO MURI W911NF-12-1-0461, NSF-MRSEC DMR-0819860, Packard Foundation and Keck grant. D. G., A. A. S., and M. T. were supported by Microsoft Research, the European Research Council through ERC Advanced Grant SIMCOFE, the Swiss National Science Foundation through the National Competence Centers in Research MARVEL and QSIT. Z. W. and X. D. were supported by the National Natural Science Foundation of China (No. 11504117), the 973 program of China (No. 2013CB921700), and the "trategic Priority Research Program (B)" of the Chinese Academy of Sciences (No. XDB07020100).

Z. W. and D. G. contributed equally to this work.

[1] G. E. Volovik, *The Universe in a Helium Droplet* (Oxford University Press, New York, 2009).
[2] T. Bevan, A. Manninen, J. Cook, J. Hook, H. Hall, T. Vachaspati, and G. Volovik, Nature (London) **386**, 689 (1997).
[3] B. Q. Lv, H. M. Weng, B. B. Fu, X. P. Wang, H. Miao, J. Ma, P. Richard, X. C. Huang, L. X. Zhao, G. F. Chen, Z. Fang, X. Dai, T. Qian, and H. Ding, Phys. Rev. X **5**, 031013 (2015).
[4] S.-Y. Xu, I. Belopolski, N. Alidoust, M. Neupane, G. Bian, C. Zhang, R. Sankar, G. Chang, Z. Yuan, C.-C. Lee *et al.*, Science **349**, 613 (2015).
[5] S.-M. Huang, S.-Y. Xu, I. Belopolski, C.-C. Lee, G. Chang, B. Wang, N. Alidoust, G. Bian, M. Neupane, A. Bansil *et al.*, Nat. Commun. **6**, 7373 (2015).
[6] H. Weng, C. Fang, Z. Fang, B. A. Bernevig, and X. Dai, Phys. Rev. X **5**, 011029 (2015).
[7] H. B. Nielsen and M. Ninomiya, Phys. Lett. **130B**, 389 (1983).

[8] S. Murakami, New J. Phys. **9**, 356 (2007).
[9] X. Wan, A. M. Turner, A. Vishwanath, and S. Y. Savrasov, Phys. Rev. B **83**, 205101 (2011).
[10] H. Weyl, Zeitschrift für Physik A Hadrons and Nuclei **56**, 330 (1929).
[11] M. A. Silaev and G. E. Volovik, Phys. Rev. B **86**, 214511 (2012).
[12] G. E. Volovik, JETP Lett. **43**, 551 (1986).
[13] J. Xiong, S. K. Kushwaha, T. Liang, J. W. Krizan, M. Hirschberger, W. Wang, R. J. Cava, and N. P. Ong, Science **350**, 413 (2015).
[14] C. Zhang, S.-Y. Xu, I. Belopolski, Z. Yuan, Z. Lin, B. Tong, N. Alidoust, C.-C. Lee, S.-M. Huang, H. Lin *et al.*, Nat. Commun. **7**, 10735 (2016).
[15] X. Huang, L. Zhao, Y. Long, P. Wang, D. Chen, Z. Yang, H. Liang, M. Xue, H. Weng, Z. Fang, X. Dai, and G. Chen, Phys. Rev. X **5**, 031023 (2015).
[16] A. A. Soluyanov, D. Gresch, Z. Wang, Q. Wu, M. Troyer, X. Dai, and B. A. Bernevig, Nature (London) **527**, 495 (2015).
[17] A. A. Burkov, M. D. Hook, and L. Balents, Phys. Rev. B **84**, 235126 (2011).
[18] T. T. Heikkilä, N. B. Kopnin, and G. E. Volovik, JETP Lett. **94**, 233 (2011).
[19] L. Lu, L. Fu, J. D. Joannopoulos, and M. Soljačić, Nat. Photonics **7**, 294 (2013).
[20] H. Weng, Y. Liang, Q. Xu, R. Yu, Z. Fang, X. Dai, and Y. Kawazoe, Phys. Rev. B **92**, 045108 (2015).
[21] Y. Kim, B. J. Wieder, C. L. Kane, and A. M. Rappe, Phys. Rev. Lett. **115**, 036806 (2015).
[22] L. S. Xie, L. M. Schoop, E. M. Seibel, Q. D. Gibson, W. Xie, and R. J. Cava, APL Mater. **3**, 083602 (2015).
[23] G. Bian, T.-R. Chang, R. Sankar, S.-Y. Xu, H. Zheng, T. Neupert, C.-K. Chiu, S.-M. Huang, G. Chang, I. Belopolski *et al.*, Nat. Commun. **7**, 10556 (2016).
[24] C. Fang, Y. Chen, H.-Y. Kee, and L. Fu, Phys. Rev. B **92**, 081201 (2015).
[25] R. Yu, H. Weng, Z. Fang, X. Dai, and X. Hu, Phys. Rev. Lett. **115**, 036807 (2015).
[26] Z. Wang, A. A. Soluyanov, J. Li, M. Troyer, and B. Bernevig (work in progress).
[27] H. Nielsen and M. Ninomiya, Nucl. Phys. **B185**, 20 (1981).
[28] H. Nielsen and M. Ninomiya, Phys. Lett. **105B**, 219 (1981).
[29] F. Arnold, C. Shekhar, S.-C. Wu, Y. Sun, M. Schmidt, N. Kumar, A. G. Grushin, J. H. Bardarson, R. D. d. Reis, M. Naumann *et al.*, Nat. Commun. **7**, 11615 (2016).
[30] J. Liu and D. Vanderbilt, Phys. Rev. B **90**, 155316 (2014).
[31] M. Hirayama, R. Okugawa, S. Ishibashi, S. Murakami, and T. Miyake, Phys. Rev. Lett. **114**, 206401 (2015).
[32] T. Bzdušek, A. Rüegg, and M. Sigrist, Phys. Rev. B **91**, 165105 (2015).
[33] Y. Sun, S.-C. Wu, M. N. Ali, C. Felser, and B. Yan, Phys. Rev. B **92**, 161107 (2015).
[34] Two of these points are at $\mathbf{k} = (0.12661133, 0.0996582, 0.21142578)$ (20 meV above E_F) and $\mathbf{k} = (0.11034922, 0.07301836, 0.14727305)$ (36 meV above E_F). Another six points are related to these by the mirror reflections M_x and M_y, and eight more points are located symmetrically to these about the $k_z = 0$ plane.
[35] T.-R. Chang, S.-Y. Xu, G. Chang, C.-C. Lee, S.-M. Huang, B. Wang, G. Bian, H. Zheng, D. S. Sanchez, I. Belopolski *et al.*, Nat. Commun. **7**, 10639 (2016).
[36] See Supplemental Material at http://link.aps.org/supplemental/10.1103/PhysRevLett.117.056805, which includes Refs. [37–60], for the details on the crystal structure of $MoTe_2$ at 100 K, first-principles calculations, the nodal lines, Weyl points, and the topological invariants. More analysis of the surface states and Fermi arcs are presented as well.
[37] B. E. Brown, Acta Crystallogr. **20**, 268 (1966).
[38] M. Vellinga, R. De Jonge, and C. Haas, J. Solid State Chem. **2**, 299 (1970).
[39] K. Ikeura, H. Sakai, M. S. Bahramy, and S. Ishiwata, APL Mater. **3**, 041514 (2015).
[40] G. Sheldrick, Bruker AXS Inc., Madison, Wisconsin (2000).
[41] G. M. Sheldrick, Acta Crystallogr. Sect. A **64**, 112 (2008).
[42] P. Blaha, K. Schwarz, G. Madsen, D. Kvasnicka, and J. Luitz, *wien2k* (Technical Universität, Wien, Austria, 2001).
[43] K. Schwarz, P. Blaha, and G. Madsen, Comput. Phys. Commun. **147**, 71 (2002).
[44] J. P. Perdew, K. Burke, and M. Ernzerhof, Phys. Rev. Lett. **77**, 3865 (1996).
[45] G. Kresse and J. Furthmüller, Comput. Mater. Sci. **6**, 15 (1996).
[46] P. E. Blöchl, Phys. Rev. B **50**, 17953 (1994).
[47] G. Kresse and D. Joubert, Phys. Rev. B **59**, 1758 (1999).
[48] C. L. Kane and E. J. Mele, Phys. Rev. Lett. **95**, 146802 (2005).
[49] A. A. Soluyanov and D. Vanderbilt, Phys. Rev. B **83**, 035108 (2011).
[50] A. A. Soluyanov and D. Vanderbilt, Phys. Rev. B **83**, 235401 (2011).
[51] R. Yu, X. L. Qi, A. Bernevig, Z. Fang, and X. Dai, Phys. Rev. B **84**, 075119 (2011).
[52] Z. Wang, Y. Sun, X.-Q. Chen, C. Franchini, G. Xu, H. Weng, X. Dai, and Z. Fang, Phys. Rev. B **85**, 195320 (2012).
[53] R. D. King-Smith and D. Vanderbilt, Phys. Rev. B **47**, 1651 (1993).
[54] M. L. Sancho, J. L. Sancho, J. L. Sancho, and J. Rubio, J. Phys. F **15**, 851 (1985).
[55] K. Momma and F. Izumi, J. Appl. Crystallogr. **44**, 1272 (2011).
[56] T. Williams, C. Kelley *et al.*, http://www.gnuplot.info (2011).
[57] P. Ramachandran and G. Varoquaux, Comput. Syst. Sci. Eng. **13**, 40 (2011).
[58] J. D. Hunter, Comp. Sci. Eng. **9**, 90 (2007).
[59] G. Gimp, User Manual, Edge-Detect Filters, Sobel, The GIMP Documentation Team, 2008.
[60] M. Albert, J. Andler, T. Bah, P. Barbry-Blot, J. Barraud, B. Baxter *et al.*, *Inkscape* (2013), https://www.inkscape.org/.
[61] D. Gosálbez-Martínez, I. Souza, and D. Vanderbilt, Phys. Rev. B **92**, 085138 (2015).
[62] P. Hohenberg and W. Kohn, Phys. Rev. **136**, B864 (1964).
[63] W. Kohn and L. J. Sham, Phys. Rev. **140**, A1133 (1965).
[64] J. P. Perdew, K. Burke, and M. Ernzerhof, Phys. Rev. Lett. **77**, 3865 (1996).
[65] I. Souza, N. Marzari, and D. Vanderbilt, Phys. Rev. B **65**, 035109 (2001).
[66] A. A. Mostofi, J. R. Yates, Y.-S. Lee, I. Souza, D. Vanderbilt, and N. Marzari, Comput. Phys. Commun. **178**, 685 (2008).
[67] D. Gresch, A. A. Soluyanov, G. Autés, O. Yazyev, B. A. Bernevig, D. Vanderbilt, and M. Troyer, Universal Framework for identifying topological materials and its numerical implementation in the Z2Pack software package (unpublished).
[68] N. Xu *et al.*, arXiv:1604.02116.